Search for Weak Neutral Currents in Nuclei

R.G.H. Robertson, R.A. Warner,* T.J. Bowles,+ P. Dyer, and R.C. Melin

As described in last year's annual report, an experiment is underway to measure the parity-violating alpha width of the 0^+, T=1 state of ^{6}Li at 3.56 MeV. The method consists of bombarding a ^{2}H target with a ^{4}He beam and observing ^{6}Li recoils at 0° in the Enge spectrograph. In the past year we have considerably refined our experimental technique, obtained further data on the non-resonant (direct capture) background, and have carried out a preliminary run on resonance with the D_2O vapor jet target recently constructed by one of us (P.D.).

Much of our effort has been directed toward reducing the background of degraded alphas on the focal plane, and improving our ability to discriminate against that background. A new detector has been constructed which incorporates several features aimed at improved pile-up rejection (see figure). It is a stopping proportional counter divided into front (ΔE) and back (E) sections by a ground wire plane. The ΔE section contains two 50 μm Ni anode wires below the median plane and above a delay-line-readout "stripe" board. The E section contains seven anode wires above the median plane. Delay-line readout of the position enables us to identify and reject events in which two alpha particles arrive simultaneously but at different locations on the detector; such events lead to pairs of time-separated pulses travelling on the delay line. Similarly, the drift velocity of primary ionization acts as a delay line in the vertical direction, and pulse-shape discrimination on the front and back wire planes can be used to reject piled-up alphas. A further advantage of placing front and back wire planes below and above the median plane, respectively, is that vertical position can be derived as well as horizontal, assuring us that the ^{6}Li group is centered on the detector in both dimensions. (Moreover, the vertical position information can be used to obtain surprisingly good timing for time-of-flight. A time resolution of 9 ns FWHM has been observed, notwithstanding the 400 ns total drift time for primary ionization. However, time-of-flight is not a useful parameter in this particular experiment because the alphas and ^{6}Li's have the same time-of-flight.)

A new electronic setup has been implemented in which leading-edge and zero-crossing times are measured for signals from both ends of the delay line and both wire planes. Those times, and the cyclotron RF, comprise the start and 8 stops for a CAMAC octal time-to-digital converter. Adding E and ΔE to the list, ten-parameter data is then written on magnetic tape. This scheme has resulted in at least a threefold improvement in pile-up rejection over our previous arrangement. The equivalent pulse-pair resolution for a single detector is now less than 250 ps.

Substantial improvements in the background of alpha particles have been made. Two quadrupoles have been added to the beam line between the switching magnet (M5) and the shielding wall of the spectrograph vault. (The additional focusing prevents the beam from filling the beam line at or before the quadrupoles in the spectrograph vault.) Highly polished brass slits replace the standard image slits and the entrance slit to the spectrograph. A second pumping station has been added to the beam line. These measures have reduced the alpha background by more than an order of magnitude.

The actual measurement of the parity-violating alpha width requires accurate knowledge of the beam energy, target composition, and target thickness. Solid targets are ruled out because of their susceptibility to deterioration and the buildup of inert layers on their surfaces. To circumvent these difficulties a target has been constructed in which D_2O vapor at about 3 atmospheres pressure is allowed to expand freely from a nozzle to form a supersonic jet. The vapor is condensed instantly on a liquid-nitrogen-cooled trap surrounding the nozzle. Approximately 200 grams per hour of D_2O can be passed through the target without perturbing the beam line vacuum. After one hour the absorption capacity of the trap is exceeded, and the D_2O must be melted and recovered, an automated procedure which takes about 40 minutes. Some development work remains to be done on this target (at 0.14 μg cm^{-2}, it is not yet thick enough, and the vapor jet occasionally is contaminated with solid or liquid D_2O particles), but a very short preliminary run with it enabled us to set an upper limit of 3×10^{-4} eV on $\Gamma_{\alpha d}$, at the 68% confidence level. This is the best upper limit yet obtained on $\Gamma_{\alpha d}$, and we expect to improve on it substantially.[1]

Information on the non-resonant capture cross-section is contained in the astrophysics section of this report.

---

*

+ Present address: Battelle Northwest, Richland, WA.

Argonne National Laboratory, Argonne, IL

1. The previous limit was 8×10^{-4} eV (E. Bellotti et al., Nuovo Cim. 29A (1975) 106).

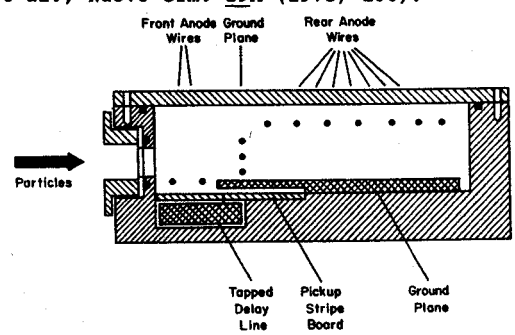

Fig. 1. Cross-sectional view of the proportional counter used in the ^{2}H(α,γ)^{6}Li experiments.

Role of the $^2H(\alpha,\gamma)^6Li$ Reaction in Big-Bang Nucleosynthesis

R.G.H. Robertson, R.A. Warner,* T.J. Bowles,+ P. Dyer, and R.C. Melin

The notable successes of the standard big-bang model of the early universe include the Hubble expansion, the 3^oK microwave background, and a quantitatively correct mechanism[1] for production of the light isotopes ^2H, $^3He(?)$, ^4He, and ^7Li. The nuclear reaction cross-sections relevant to big-bang nucleosynthesis have all been experimentally investigated with the sole exception of $^2H(\alpha,\gamma)^6Li$. This reaction has a low cross section by virtue of selection rules which hinder E1 and M1 transitions, leaving E2 as the lowest order allowed multipolarity. As a consequence, no successful observation of the radiative capture has been reported, and it has been necessary to rely on theoretical estimates for the capture cross-section. The estimate currently in use[1] is based on a direct capture (DC) calculation by Tombrello wherein M1 is presumed to be the dominant multipolarity at astrophysical energies.[2] Fowler[2] has independently estimated the contribution from the well-known 3^+ resonance in ^6Li, and has found it to be negligible (≈1% of the M1 DC). Using these estimates, Schramm and Wagoner find[1] that ^6Li production is a strongly decreasing function of the density of the universe, and is small (compared to cosmic ray production) at densities above the lower limit set by the observable matter in galaxies (see Fig. 1). However, if the capture cross section were significantly larger (4x), then the ^6Li abundance could significantly constrain the minimum density of the universe. The minimum baryon density, as Schramm has pointed out,[3] limits the number of possible species of massless neutrinos, presently fixed at less than five.

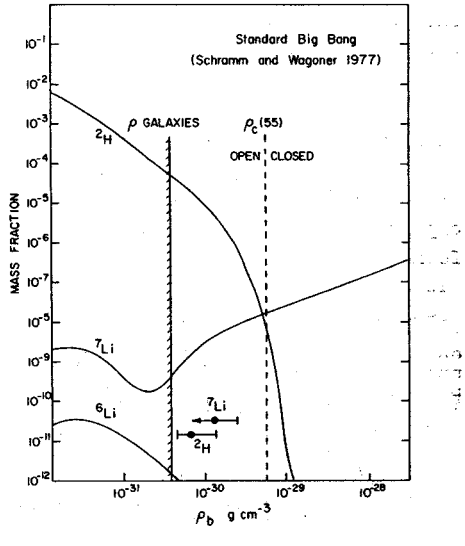

FIG. 1. Predicted mass fractions for ^2H, ^6Li, and ^7Li in big-bang nucleosynthesis (from Ref. 1). $\rho_c(55)$ is the critical density needed to close the universe if the Hubble constant is 55 sec km^{-1} Mpc^{-1}, and ρ galaxies is the minimum density inferred from observable matter.

In our investigation of the parity-violating alpha width of the 0^+, T=1 state of ^6Li (described in last year's report and elsewhere in this report) we have successfully observed the capture reaction at incident α energies from 5.4 to 25 MeV. The present status of our data is summarized in Fig.2.

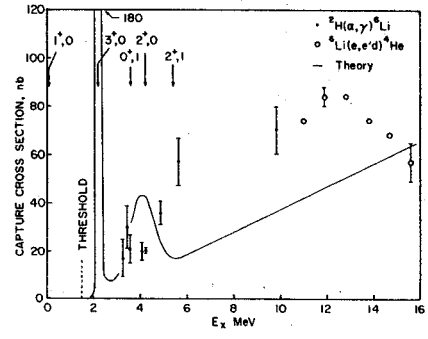

FIG. 2. Cross section for the radiative capture process $^2H(\alpha,\gamma)^6Li$.

These data were taken several months ago, prior to several improvements in the experimental technique, and it is possible that we may be able to increase significantly the quality of the lower points.

At higher energies there exist electrodisintegration data from Saskatoon.[4] Those data are shown on the figure converted to the equivalent capture cross section, but in making that conversion it has been assumed that the E0 contribution to the electrodisintegration is negligible. The solid curve is a direct capture calculation by the Saskatoon group.[4] In view of its obvious deficiencies in the region where data exist, we are reluctant to use it to extrapolate into the astrophysical region. We hope to improve on the calculation, but it is a complex problem because of the presence of broad resonances, several multipolarities, and significant intranuclear contributions to the capture.

Comparing experiment with the low-energy extrapolation formula of Schramm and Wagoner,[1] we find experimental cross sections to be perhaps 2-3 times larger, but little stock can be placed

in this because the extrapolation formula is not valid at such high energies and assumes M1 is the dominant multipolarity. Experimentally we find that, at E_α=8.1 MeV at least, the capture is largely E2.

---

* Present address: Battelle Northwest, Richland, WA.
+ Argonne National Laboratory, Argonne, IL.

1. D.N. Schramm and R.V. Wagoner, Ann. Rev. Nucl. Sci. 27 (1977) 37.
2. W.A. Fowler, private communication.
3. D.N. Schramm, paper presented at Neutrinos–78 conference, Purdue University, 1978.
4. D.M. Skopik, E.L. Tomusiak, E.T. Dressler, Y.M. Shin, and T.J. Murphy, II, Phys. Rev. C 14 (1976) 789.

Production and the Spin Dependence of the PP Total Cross Section

G.N. Epstein and D.O. Riska

The total cross section difference for polarized proton-proton scattering: $\sigma(\uparrow\downarrow)-\sigma(\uparrow\uparrow)$ was calculated assuming it to be dominated by production by one or two Δ resonances.[1] The production mechanism for the resonance was assumed to involve pion and ρ-meson exchange. Qualitatively reasonable agreement with data [2] could be obtained by adjusting the mass scale in the meson-nucleon form factors.

1. G.N. Epstein and D.O. Riska, A. Physik A283 (1977) 193
2. W. DeBoer et al., Phys. Rev. Lett. 34 (1974) 558.

Pionic Disintegration of the Deuteron[1]

M. Brack,* D.O. Riska, and W. Weise**

The total cross section for the reaction $\pi^+d\to pp$ has been calculated using a model for the absorption operator involving pion and ρ-meson rescattering. The effect of the width of the ρ-meson was studied, as was the effect of including hadronic form factors of the meson-nuclear vertices. Since the effect of the ρ-meson exchange on the cross section is similar to that of form factors, different values for the ρ-nucleon coupling constants can be used if the mass scale parameter in the form factors is adjusted in a compensatory way.

* Present address: S.U.N.Y., Stony Brook, NY.
** Present address: Regensburg.

1. M. Brack, D.O. Riska, and W. Weise, Nucl. Phys. A287 (1977) 475.

Pion Absorption in Nuclei

G.F. Bertsch, J. Chai, C.M. Ko, and D.O. Riska

As pions cannot be absorbed on free nucleons, nuclear pion absorption involves at least a two-nucleon mechanism. This may either be viewed as absorption on a single but bound nucleon or as an explicit two-nucleon absorption mechanism. We have shown that most of the empirical nuclear absorption rates (i.e. the absorption rates deduced from the level widths of pionic atoms) can be explained in terms of a model for the absorption operator which also leads to a good description of the total cross section for the fundamental reaction $\pi^+d\to pp$. In this model S-wave pion absorption takes place by a mechanism involving pion rescattering and P-wave absorption by a more complicated mechanism involving pion and rho-meson rescattering following excitation of an intermediate Δ_{33} resonance.

The threshold absorption rates for ^2H, ^4He, ^{12}C, ^{16}O, and ^{20}Ne have been calculated and compared to experiment. While the calculated absorption rate for ^2H is in excellent agreement with the experimental value for the deuteron, the calculated values are 20-30% too small in the other nuclei. The parameters ImB_o and ImC_o which describe the strength of the absorption parts of the pion-nucleus optical potential have also been calculated. The value for ImB_o seems to be too small by $\approx$25%, whereas the value for ImC_o is in reasonable agreement with the phenomenological values obtained from pionic atom level widths. The energy dependence of these parameters has also been calculated and found to depend more on the structure of the rescattering vertex than on the nuclear matrix elements.

Many-Body Exchange Current Contributions to the Tri- and Four-Nuclear Change Form Factors[1]

D.O. Riska and Mark Radomski

We have constructed the three and four-body pion and ρ-meson exchange charge operators illustrated by the diagrams:

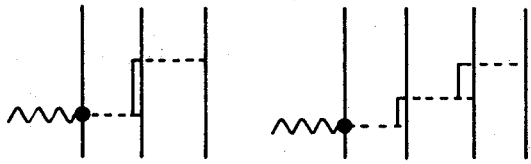

The intermediate pion-nucleon rescattering vertex was described by an S-wave and a P-wave component constructed from phenomenological Lagrangians. The model is essentially the same as that commonly used in the construction of the nuclear three-body force. Qualitatively the effects on the charge form factors of ^{3}He and ^{4}He of the pion exchange three and four-body operators is similar to that of the two-body pion exchange operator but somewhat smaller. The effect of the ρ-meson exchange mechanism is to strongly reduce the three and four-body effects but to increase the two-body exchange effect. The conclusion is therefore that once ρ-meson exchange is taken into account many-body operators other than the two-body ones will be of little significance.

---

1. D.O. Riska and Mark Radomski, Phys. Rev. C 16 (1977) 2105.

Exchange Current Corrections to Nuclear Charge Densities

J.W. Negele* and D.O. Riska

It has previously been shown that the pion exchange correction to the nuclear charge operator leads to a large effect on the charge form factors of the three and four-nuclear systems,[1,2] which serves to reduce the discrepancy between the theoretical and experimental values. We have therefore investigated the effect of this charge operator:

$$\rho(1,2)=\frac{q^2}{8m^3}\,[F_1^S\,\tau^1\cdot\tau^2 + F_1^V\tau^2{}_3]\,\frac{\sigma^1\cdot q\sigma^2\cdot \ell}{\mu^2+\ell^2} \qquad (1)$$

on the charge densities of closed shell nuclei:[3] In (1) q is the momentum transfer and ℓ the momentum of the exchanged pion.

The matrix element of (1) was calculated for ^{12}C, ^{16}O, ^{40}Ca, ^{48}Ca, ^{90}Zr, and ^{208}Pb using density dependent Hartree-Fock wave functions. In every case considered we found that the pion exchange correction serves to reduce the discrepancy between the calculated charge densities and the values obtained from the electron scattering data in the central region of the nucleus. For example, in ^{208}Pb the inclusion of the exchange correction reduces the χ^2 for the fit to the total supply of available data from 4822 to 2683. The correction is, however, far from large enough to be able to completely remove the discrepancy.

---

* Present address: M.I.T., Cambridge, MA.

1. W. Kloet and T. Tjon, Phys. Lett. 49B, (1974) 419.
2. J. Borysowicz and D.O. Riska, Nucl. Phys. A254, (1975) 301.
3. J.W. Negele and D.O. Riska, Phys. Rev. Lett. 40, (1978) 419.

Purification and Use of ^{13}N in Studies of Denitrification and Dissimilatory Nitrate Reduction

J.M. Tiedje, R.B. Firestone, M.S. Smith, W.H. Caskey, M.K. Firestone and M.R. Betlach

Denitrification is the process by which bacteria in nature convert nitrate to N_2 and N_2O, nitrogen forms that are unavailable to biological organisms (except for the restricted case of diazotrophs). This loss is particularly significant since nitrogen is the most limiting nutrient for productivity in both soils and oceans. In the agricultural case it is known that only one-half of the N fertilizer reaches the grain crop. Of that lost at least one-half is estimated to be lost to denitrification. This is calculated to be 12 to 15 million tons of fertilizer nitrogen world wide.[1] The importance of this process and the need for more basic research has been formally recognized by several scientific groups studying the world food problem.[2,3] ^{13}N provides a direct and sensitive approach to studying denitrification not possible with other methods. Major advantages of ^{13}N are that one can measure denitrification rates over the short-term and that N_2 can be measured directly in the presence of the natural atmosphere.

Previously we reported on the methods we had developed to measure the inorganic species of ^{13}N.[4] We have now characterized the typical ^{13}N species mixture formed under our routine irradiation conditions. We use a water target and the ^{16}O (p,α) ^{13}N reaction. The species and range in composition is as follows: NO_3^-, 75-90%; NO_2^-, 5-10%; NH_4^+, 5-25%; N_2, trace; N_2O, trace; NO, undetectable. The methods used to purify this mixture to the desired product and their efficacy is summarized in Table 1. Methods 2, 4 and 5 are most commonly used and are reliable. The HPLC method provides us with both purified $^{13}NO_2^-$ and $^{13}NO_3$, the two denitrification substrates.

a. Rates of denitrification

An advantage of ^{13}N over ^{15}N (stable Isotope) is the much higher sensitivity the former provides. Thus, ^{13}N can be added in amounts which do not affect the natural concentration, and thus does not yield erroneous rates of denitrification. An example of the temporal pattern of gas production from a soil to which $^{13}NO_2^-$ had been added is shown in Figure 1. The sterile soil serves as a control and shows that gas production is biologically catalyzed. In this example the concentration of NO_2^- was low enough so that the total electron acceptor pool was converted to N_2O (26%) and N_2 (74%) within 40 min. From the linear portion of plots like these, rates of denitrification can be calculated. Examples of some of these rates for different freshly collected soils are shown in Table 2. The ratios of the rates of production of N_2O relative to total gas can also be determined.

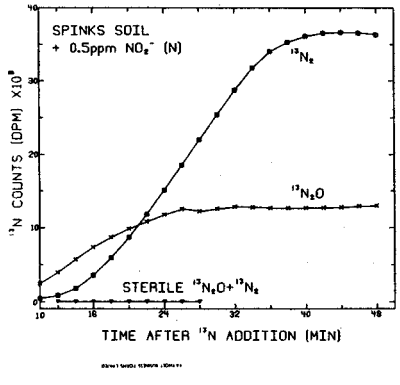

Fig. 1. ^{13}N gases produced from soil incubation in gas stripping system after adding a mixture of 0.5 ppm $^{14}NO_2^-$-N (final concentration) and 3.7 mCi $^{13}NO_2^-$-N (5×10^{-8} ppm) to a soil slurry. Control of autoclaved soil shows no labeled gas was produced.

b. Dissimilatory reduction of NO_3^- to NH_4^+

A second fate of nitrate in oxygen stressed environments can be the dissimilatory reduction of nitrate to ammonium, a process that is obscure in the literature and thus neglected by many scientists. The importance of the pathway is that it competes for nitrate with denitrification but produces a product useful to biological organisms. Our interest is to gain a fundamental understanding of the process and what controls it so that it might be used to compete against denitrification and thus conserve nitrogen.

^{13}N was necessary in our studies since the organisms catalyzing this reduction require a medium containing a complex mixture of organic nitrogen compounds, and without a label it was impossible to distinguish NH_4^+ coming from NO_3^- from that coming from organic nitrogen. Table 3 shows the effect of several compounds, which from biochemical knowledge of nitrogen metabolism, might be expected to affect this pathway. With the exception of NH_4^+, none had a significant effect. This suggests that the molecular basis for regulation of the pathway is different from that for other pathways of nitrogen metabolism.

^{13}N has allowed us to obtain short-term rates of denitrification, in effect to assay for the natural enzyme activity. With such an assay we have been able to determine rapid changes in denitrification rates and products due to environmental factors, eg. O_2, pH, NO_3^-, NO_2^- and available carbon. The isotope has also allowed us to begin an investigation of the physiology of dissimilatory nitrate reducers, organisms which could be very useful for conserving nitrogen in food producing environments.

1. Tiedje, J.M. Meeting World Nitrogen Needs-Problems and Perspectives, Symposium on Nitrogen, AAAS Annual Mtg, Washington, D.C. (1978)

2. Enhancement of Food Production for the United States-World Food and Nutrition Study. Report of National Academy of Sciences, Washington, D.C. (1975)
3. Organizing and Financing Basic Research to Increase Food Production. Office of Technology Assessment, Congress of United States. (1977)
4. Firestone, R.B. et al., 1976-77 Annual Report of MSU Cyclotron Laboratory, p. 82.

Table 1. Summary of methods used to purify irradiation mixture for desired radiochemical species.

No	Method of purification	Species removed	Desired product	Nominal* purity (%)	Yield (mCi)	Time required† (min)
1.	Sparge with He for 4 min	$^{13}N_2$, $^{13}N_2O$	^{13}N ions†	> 99.9	2-4	6
2.	Add 0.1 ml of 0.01 N NaOH, evaporate to dryness twice$	above + $^{13}NH_3$	$^{13}NO_3^-$ + $^{13}NO_2^-$≠	99.8	2-4	10
3.	Above, then adjust pH to 3$ and add 1.5% H_2O_2, evaporate$	$^{13}NO_2^-$ → $^{13}NO_3^-$	$^{13}NO_3^-$≠	98	2-4	15
4.	Separation by HPLC, ∿220 to 250 sec fraction$	$^{18}F^-$, $^{13}NO_3^-$, $^{13}NH_3$	$^{13}NO_2^-$	99	0.3-1	15
5.	Separation by HPLC, ∿280 to 310 sec fraction$	$^{18}F^-$, $^{13}NO_2^-$, $^{13}NH_3$	$^{13}NO_3^-$	> 99.9	0.5-2	15

* Determined by HPLC.

† Time from end of bombardment until product is ready for use in an experiment.

≠ $^{18}F^-$ remains in product solution.

$ Methods developed in conjunction with C. P. Wolk and J. C. Meeks

Table 2. Examples of rates of denitrification and ratios of products for different soils and different periods of anaerobiosis determined with ^{13}N.

Soil	Time after anaerobiosis (hours)	Denitrification rate (nmoles $gas \cdot g^{-1} \cdot min^{-1}$)	Ratio of products $\delta N_2O/\delta (N_2+N_2O)$
Brookston	0-1	0.51	0.05
Brookston	2-3	0.70	0.34
Carlisle	4-5	2.15	0.48
Spinks	7-9	0.10	0.74

Table 3. Effect of various compounds on the reduction of $^{13}NO_3^-$* to $^{13}NH_4^+$ by resting cells of Clostridium KDHS2.

Inhibitor	$^{13}NH_4^+$ produced (log dpm)†
Heat-killed cells	none
None	4.83
NH_4^+	3.19
Glutamate	4.91
Glutamine	4.49
Methionine Sulfoximine, 0.01 mM	4.14
Methionine Sulfoximine, 10 mM	5.00
Azaserine, 1.0 mM	4.97
$SO_3^=$, 3.5 mM	5.16
$SO_4^=$, 3.5 mM	4.58

* Incubated at room temperature for 20 min with 1.0 µg unlabeled NO_3^--N.

† Standard error calculated from analysis of variance is 0.54 for each mean.

Use of ^{13}N to Determine the Gaseous Denitrification Products

M.K. Firestone, R.B. Firestone, M.R. Betlach and J.M. Tiedje

The final products of denitrification are N_2O and N_2 with the latter assumed to be the major product. Nitrous oxide was a neglected product because it was thought to be innocuous. Recently, however, some atmospheric chemists have indicated that N_2O, via its photochemical product NO, catalyzes destruction of the ozone layer. The major source of N_2O is denitrification in nature and there is concern that man's activities are increasing the amount of N_2O in the atmosphere. The factors which control the proportion of N_2O vs N_2 and the ease with which it is lost from the denitrifying cells were unanswered questions of basic importance to the N_2O issue. These questions could most directly be answered by use of ^{13}N.

a. Exchange of $^{13}N_2O$ with nonlabeled pools of N_2O

If N_2O is freely diffusible from the site of active denitrification then any factor which either slowed the reduction of N_2O to N_2 or enhanced the steps forming N_2O would result in increased production of N_2O. This question was investigated by adding $^{13}NO_3^-$ to soils containing natural populations of denitrifying cells together with increasing concentrations of $^{14}N_2O$. The N_2O produced by denitrification of the added $^{13}NO_3^-$ would be labeled as $^{13}N_2O$. If it was freely diffusible it should mix with the $^{14}N_2O$ outside the cell. The results, shown in Figure 1, clearly indicate that N_2O is freely diffusible. As the $^{14}N_2O$ concentration increased, the amount of $^{13}N_2O$ accumulated in the extracellular pool increased and the amount of $^{13}N_2$ produced decreased.

b. Factors affecting the ratio of N_2O/N_2

We have found that increasing concentrations of NO_3^-, NO_2^- and O_2 all increase the proportion of N_2O produced as shown in Table 1. Nitrite was always a stronger effector than nitrate. Oxygen usually but not always showed a positive effect on N_2O production. However, work with pure cultures of denitrifiers showed a consistent positive effect of O_2 on N_2O production.

The other major factor that controls the N_2O/N_2 ratio is the length of time soil experiences oxygen stress. The period from 6 hours to 1 1/2 days showed maximum N_2O production, sometimes reaching 90% of the product gases. Thereafter more N_2O reductase was synthesized and the rate of net N_2O production diminished. A final factor identified as affecting this ratio is pH. A decrease in pH caused an increase in N_2O.

c. Exchange of NO from denitrifying cells

Though NO is thought by most to be an intermediate in denitrification, it is a point of contention by others. Only limited and inconclusive information exists to support the interpretations. ^{13}N, however, provides a more direct approach to the question. $^{13}NO_3^-$ and $^{13}NO_2^-$ were used as substrates in experiments analogous to those described for N_2O exchange. When high (approx. 0.1 atm) but not low concentrations of ^{14}NO was added, ^{13}NO was produced (Table 2). NO production by denitrifying cells is normally not observed and thus it is assumed to be an enzyme bound intermediate. In this case higher concentrations of NO appeared to be effective in exchanging some of the ^{13}NO from its binding site.

Since NO can also be formed chemically from NO_2^- at lower pHs (i.e. HONO) it was necessary to rule out this mechanism as the source of the ^{13}NO. Three approaches were used - use of purified $^{13}NO_3^-$ and $^{13}NO_2^-$, use of a bacterium, Flavobacterium, which does not excrete NO_2^-, and use of sterilized soils as controls. All supported the conclusion that ^{13}NO was formed directly from the denitrification pathway (Table 2). The sterilized control did show some ^{13}NO but it was an order on magnitude less than for the non-sterilized soils. Our evidence thus strongly supports NO as being a denitrification intermediate.

The N_2O and NO exhange experiments could not have been done without a radioactive nitrogen label and thus represent an example of a valuable and unique use of this isotope. The questions of N_2O diffusibility and NO as an intermediate are central to the fundamental understanding of denitrification as well as being of practical importance to resolving the concern over ozone destruction. Studies on factors determining the ratio of N_2O/N_2 can be approached by other methods but only ^{13}N methods allow direct and rapid detection of the rate of production of the two gases under more natural conditions.

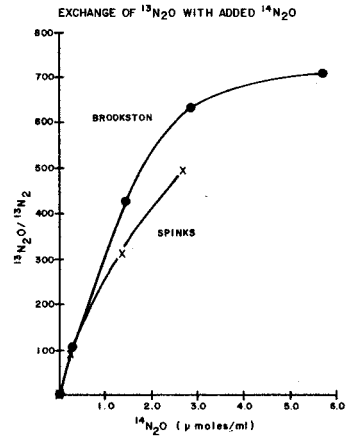

Fig. 1. Exchange of $^{13}N_2O$ produced from denitrification of $^{13}NO_3^-$ with $^{14}N_2O$ in extracellular pool for two different soils.

Table 1. Effect of NO_3^-, NO_2^- and O_2 concentrations on the ratio of denitrification products.

Effector	Concentration	$\frac{^{13}N_2O}{^{13}N_2}$
NO_3^{-a}	0 ppm	0.02
	0.5	0.06
	2	0.10
	20	0.13
NO_2^{-a}	0 ppm	0.24
	2	0.48
	6.7	1.55
	20	5.63
O_2^b	0 atm	0.42
	0.016	0.89
	0.163	1.48

[a]Done with continuous flow gas stripping system
[b]Done in sealed flasks and analyzed by gas chromatograph-proportional counter

Table 2. Exchange of ^{13}NO produced by soil and a denitrifier from $^{13}NO_3^-$ and $^{13}NO_2^-$ with a ^{14}NO pool

^{13}N Substrate	^{13}NO	Total ^{13}N gas	$\frac{^{13}NO}{\text{Total } ^{13}N \text{ gas}}$
	------dps x $10^3 \cdot ml^{-1}$------		
Brookston:			
$^{13}NO_2^-$	46.0*	47.0	0.98
$^{13}NO_3^-$	54.2	59.0	0.92
Flavobacterium sp.:			
$^{13}NO_2^-$	21.0*	27.5	0.77
$^{13}NO_3^-$	28.4	30.3	0.94

* ^{14}NO added was 0.163 atm in soil and 0.15 atm in pure culture.

50 MeV Cyclotron Developments

P. Miller, H. Laumer, G. Stork, M. Mallory, H. Blosser, and J. Nolen, Jr.

I. Heavy Ion Developments

The short lifetime (2-4 hrs.) of tantalum cathodes in the heavy ion source requires that the ion source be serviced many times during one experiment. The observation of a low sputtering yield for hafnium being bombarded by argon ions in our target-making apparatus led us to try cathodes made of hafnium metal in the heavy ion source. Initial test runs using CO arc support gas were very encouraging. One set of cathodes lasted 33 hours while producing $^{12}C^{4+}$ at normal intensity. Subsequent testing has revealed that the arc power is more critical than with tantalum. The hafnium cathodes melt at an arc power level somewhere above 2 kW in our source. Comparison of beam intensity and cathode lifetime was done between hafnium and tantalum cathodes, with all other parts in the source being the same. Generally, it seems that hafnium cathodes last much longer than tantalum (≈10x), but they yield less beam intensity (see Table I). The external beam intensity was 40% to 55% of the tabulated internal beam.

Table I. Beam intensity (probe electrical current at R=29", for source slit .125" wide, CO arc support gas).

	$^{12}C^{4+}$	$^{16}O^{5+}$
Hf cathodes	2-4 μA	.2 μA
Ta cathodes	15-30 μA	3 μA

Some similar tests were attempted for Li^{3+} ions made by sputtering from a recess in the ion source by rf back-bombardment. A 42 MeV $^{7}Li^{3+}$ beam ran for about 6 hours, until the LiF charge was exhausted. It was not possible, however, to obtain usable beams of 75 MeV $^{6}Li^{3+}$, which is the highest lithium energy, because the back bombardment was much more vigorous with the higher dee voltage required at that energy. With Hf cathodes, an effective compromise between the following conflicting requirements appeared to be impossible: high enough gas flow to maintain the arc when the dee voltage is off (as for a spark), and low enough gas flow to reach arc conditions that produce 3^{+} ions with rf on.

Dee sparking increases very noticeably when the heavy ion source is on and the dee voltage is high. The effect is most severe when a source is first inserted into the cyclotron, but it is erratic and non-repeatable. Often episodes of frequent sparking will come and go in the middle of a run. A special water cooling line was added to the second harmonic puller, since the puller was being heated visibly by ions from the source. The air lock pumping hose was also replaced with a larger diameter metal tube for better outgassing of the source in the air lock. Unfortunately, there is no clear sign of any improvement in sparking. We also note that dee sparking seems to be sensitive to adjustment of arc parameters. There is no sparking problem even with as large a gas flow as 3 cc/min. when the arc is not running.

Deflector Insulator Experience

One of the two insulators supporting the electrostatic deflector has failed repeatedly and usually has marks in the cyclotron median plane which seem to be damage from bombardment by low velocity ions drifting in the crossed electric and magnetic fields that exist there. An insulator with a hole in the median plane to let these ions pass safely was installed and ran for about one month without trouble. The test was terminated by the breakdown of the unmodified insulator. There is evidence of local discharges on the insulator surfaces where they touch the electrodes. A new insulator arrangement is being designed using quartz rods, instead of boron nitride, to maintain a cleaner surface. The insulators are out of the midplane.

Glow discharge cleaning of the deflector with an alternating current arc in hydrogen gas has become a standard conditioning procedure. Apparently this removes contaminants from the electrode surfaces which reduce the voltage that the deflector will support. The spark anodes will usually last several months before requiring replacement. The glow cleaning is done after each vacuum break. The flow of hydrogen gives a pressure of 300 μ with the roughing pump operating alone (Roots blower booster pump is turned off). The arc parameters are 300-350 VAC at .1 to .2 A from a variable transformer with a 1 K current limiting series resistor. The glow is done for about 1 hour, half with magnet off and half with magnet current = 10 A.

Computer Control

A program has been developed to scan the differential probe across the last few turns of the internal beam and display to the operator the width of a selected turn. Normally one makes a visual estimate of this quantity from a strip chart record of the differential probe current. Small changes of either the main magnet current or the radio frequency are made until the setting is found that gives the sharpest turn (minimum width). Fig. 1 is a sample display of the turn pattern and the calculation of the width of a particular turn chosen for tuning.

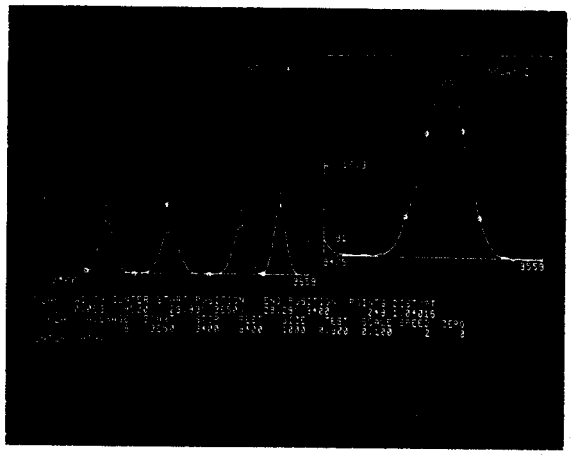

Fig. 1. Photograph of the computer terminal display of the turn pattern. The radius increases toward the right; differential current is plotted upward. The left hand box contains a scan of the last 4 turns before the beam is extracted. It covers the radius interval from 29.89 inches to 29.29 inches. The turn marked with a star above it is plotted with higher resolution in the box on the right. Its width has been found to be .063 inches (average of full width at 25% and 75% peak). The points used to determine the width have been marked on the expanded plot.

The problem of reducing the many points in a line profile to a single number (width) indicating the quality of the tune has not been treated well enough to take advantage of the high precision possible in computer processing. The present algorithm for characterizing the width of a turn has the correct qualitative response to the non-symmetrical tails which appear quickly and fill in the spaces between turns as the cyclotron is detuned, but some significant details that the person instantly (and often unconsciously) recognizes are ignored in the computer. Another problem with the computer method is that there is a time lag between the command to scan the probe and the appearance of the plot, which is not the case with the conventional chart recorder display. As a result the tune-up procedure is not done faster or better with computer assistance.

Magnet Resistance Interlock

A total resistance interlock has been added to the power supply for the magnetic channel coil to supplement the water flow switch for coil protection. The resistance of the load is computed by analog division of the power supply output voltage by the output current as measured by the precision shunt for the power supply regulator. The load resistance (typically .28 to .31 Ω, depending on temperature) is displayed on a meter and continuously monitored by a discriminator which turns off the power supply if high resistance is detected. The discriminator is set at about 5% above the normal maximum resistance. The temperature coefficient of the load resistance is $.0036^{\circ}C^{-1}$ measured under constant current conditions with the temperature of the cooling water being varied externally. This agrees with the value for copper of $.0038^{\circ}C^{-1}$. At full power an average temperature increase of less than $10^{\circ}C$ will activate the interlock. The normal outlet water temperature is $\leq 74^{\circ}C$ (with $32^{\circ}C$ inlet water).

The resistance sensor offers protection against faults other than an overall loss or reduction of water flow, such as corrosion of the electrical connections. The individual water circuits in this coil cannot be fitted with independent water pipes and flow switches, due to mechanical requirements for access to the cyclotron. The resistance interlock might protect the copper conductor from melting if one water circuit became clogged, although the temperature of the affected segment must rise several hundred degrees to trip the interlock.

Measurement of Incoherent Beam Emittance

P.S. Miller, E. Kashy, and J.A. Nolen, Jr.

The television-scintillator beam detection system used for rapid tuning of the beam transport system to a "dispersion match" for the magnetic spectrograph is described elsewhere in this annual report. It allows us to make, in a short time, a direct measurement of the incoherent radial emittance of the accelerator beam. This quantity was inferred by Blosser[1] from standard emittance measurements on the dispersed beam by comparing them in detail with calculations giving the effect of dispersion on the beam distribution. The result for 40 MeV protons was 0.7 mm-mrad. A subsequent (unpublished) measurement with refined apparatus reduced the value to 0.3 mm-mrad. The present direct measurements confirm this more recent result. The method has also been applied to two other beams, 70 MeV $^{3}He^{2+}$ and 77 MeV $^{12}C^{4+}$.

The direct beam was brought through the spectrograph to a focus on the scintillator in the focal plane. The beamline quadrupoles were adjusted to give a dispersion match, indicated by minimum line width. The spot size Δx and the divergence angle $\Delta\theta$ were measured. The emittance area of the beam ellipse is $\pi(\Delta x\ \Delta\theta)/4$, where Δx and $\Delta\theta$ represent the full axes of the ellipse.

The angular divergence of the beam was measured with a transversely movable probe located 22 inches upstream from the focal point in the camera box of the magnetic spectrograph. The probe consisted of a tantalum plate with an attached .030" diameter tungsten wire that was clamped at one end in a bracket attached to the plate. As the probe was moved across the beam the current from it was measured. The wire signal gave a direct measure of the beam profile, but was subject to broadening from imperfect wire alignment. The occultation of the beam by the edge of the plate gave a more reliable measure of the beam width. The positions where 10% and 90% of the beam was transmitted were taken to define the divergence angle (includes 80% of the beam). Simultaneous strip chart records of the probe current and the beam current transmitted past the focal plane to the Faraday cup are shown in Fig. 1.

The line width was measured from the television display of the scintillator in the spectrograph focal plane. The full width of the beam-spot was used. The precision is ±.005 mm for the high magnification used for the proton and ^{3}He measurements.

The last column of Table I gives the emittance for each of the beams measured. The ion source slit width W_s and the line width on the focal plane W_{fp} are given for reference.

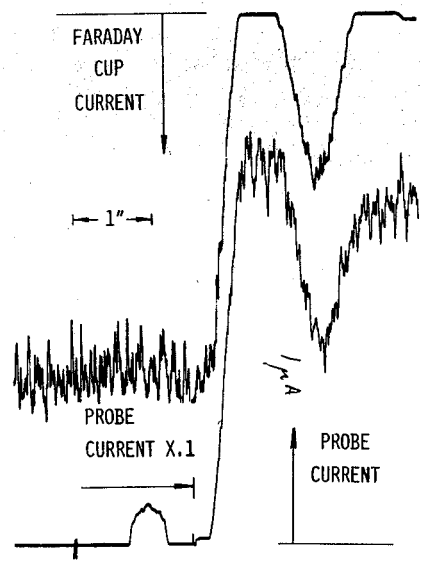

Fig. 1. Sample data for divergence angle measurement. Probe is scanned transverse to beam direction at constant speed (scale for one inch of probe motion is shown). Probe current (lower trace) increases upward; Faraday cup current (upper trace) increases downward. Beam intercepted by the probe disappears from the total Faraday cup current. Probe current amplifier sensitivity is increased by a factor 10, while wire portion of probe is in the beam, as shown in the lower left corner of the figure. The large valley in both traces on the right side of the figure is a result of the beam passing through some slots that were cut in the center of the probe plate for another experiment. The sloping parts of the traces near the center of the figure are used to measure the divergence angle.

Table 1. Incoherent Radial Emittance Data

E (MeV)	Ion	W_s (inches)	W_{fp} (mm)	Δx (mm)	$\Delta\theta$ (mrad)	$\pi/4\ \Delta x\ \Delta\theta$ (mm-mrad)
40	protons	.008	.076	.054	21	.886 (0.28π)
41	"	.008	.088	.062	18	.879 (0.28π)
40	"	.008	.041	.030	15	.353 (0.11π)
70	$^{3}He^{2+}$	.019	.121	.086	20	1.351 (0.43π)
77	$^{12}C^{4+}$	.065	.25	.177	22	3.058 (0.97π)
40	protons	.008	.038	.027	--	-------

Evidence of an intermittent short circuit in the coil of the magnetic channel in the cyclotron was recently found and the problem was corrected. The data in the third line of the table were measured after that repair. The line width agrees with an older line width done in a similar way (given in the last line of the table) and also agrees within 20% with the narrowest line widths recorded on plates or other detectors in scattering experiments.[2]

Since there is a unique optical path through the cyclotron and beam transport system to the focal plane and since coherent energy variations are cancelled, it is possible to make an image of the ion source slit on the focal plane of the spectrograph. Fig. 2 is a plot of line width versus the ion source slit width for the data in Table I. The line through the data obtained when the magnetic channel may have been producing some extra broadening of the line does not extrapolate to zero image width at zero source width. If the line is translated downward to pass through the proton data under good conditions, the relation becomes more like the ideal one for a linear optical system.

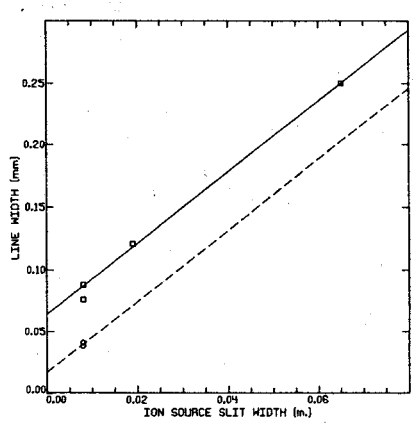

Fig. 2. Line width of image in spectrograph focal plane versus ion source slit width. Dashed line is drawn with the same slope as the solid line. In the absence of aberrations and instrumental broadening effects, the line would pass through the origin if an image is formed.

1. H.G. Blosser, Proc. of 5th International Cyc. Conf., Sept. 1969, Butterworths (1971) 257.
2. J.A. Nolen, Jr. and P.S. Miller, Proc. of 7th International Cyc. Conf., Sept. 1975, Birkhäuser (1975) 249.

Fast Resolution Optimization in a Magnetic Spectrograph

E. Kashy, P.S. Miller, and J.A. Nolen, Jr.

We have developed a technique for quickly tuning accelerator and beam optics parameters to obtain high resolution in a magnetic spectrograph, and which has applications in accelerator, beam transport, and magnetic spectrograph diagnostics. The procedure consists of viewing the beam at two positions, at the target and on the focal plane of our Enge split-pole spectrograph which is positioned at 0^{o}. Two television cameras are used and the beam is made optically visible by MgO scintillators deposited on thin aluminum foil.[1] Fig. 1 shows the arrangement at the focal plane. A 16 mm projector lens (focal length = 75 mm) is placed so that the scintillator is on its focal plane. The (approximately) parallel rays emerging from that lens enter a second lens, a zoom lens with focal length variable from 30 to 300 mm. The parallel rays between the two lenses allow movement of the focal plane (which also moves the 16 mm lens) without changing the optical focus of the beam image on the scintillator. All beam and spectrograph controls are at the console, and the procedure is then simply to (1) focus the beam on the target with the desired dispersion for the energy matching condition, and (2) adjust the various elements until the narrowest possible line is obtained in the focal plane of the spectrograph.

The results so far have been a line width for a 40 MeV proton beam of 1.5 keV (base), i.e. $p/\Delta p$ = 53,000. For heavy ion beams, we have so far tried only the 77 MeV ^{12}C beam and have observed line widths of 9-16 keV. Thus, tuning serves to test the potential that a particular accelerator-magnetic spectrograph has of achieving high resolution, since no target is involved in the procedure. The technique has also been extended (by simultaneously measuring divergence) to set an upper limit on the incoherent beam emittance,[2] as the dispersion of the beam approaches zero at the spectrograph focal plane in the process of tuning for the narrowest possible lines. While we are still studying the applications of this tuning procedure, it is already clear that it serves very well for testing target thickness and uniformity. By placing the target in the beam and viewing the beam image, the energy displacement of the beam as well as the increased line width can be readily measured. Various targets can be compared before a choice is made of the most suitable. For heavy ions, the combination of energy loss straggling, non-uniformity, and angular straggling due to multiple scattering are dominant effects in limiting energy resolution. At 0^{o}, contributions from the first two of these effects are measurable since there is no contribution from the angular effect. Heavy ion target effects are discussed by Erskine.[3]

Another interesting result is the measurement of certain spectrograph aberrations. By rotating the spectrograph a few degrees on either side of zero degrees, the resulting beam image motion can easily be recorded. In addition to giving the best "zero degree" definition of the spectrograph, quadratic and cubic aberration can be measured from data such as those shown in Fig. 2. There, the image motion along the focal plane is plotted as a function of spectrograph angle for three different values of the focal plane position, near the predicted best position of that plane.

1. J.A. Nolen, Jr., submitted to Nucl. Instr. and Methods.
2. P.S. Miller, E. Kashy, and J.A. Nolen, Jr., to be published as contribution to Cyclotron Conference, Bloomington, IN, August, 1978.
3. J.R. Erskine, Fourth Annual Conference of the Nuclear Target Development Society, Argonne, IL 1975, p. 141.
4. J.E. Spencer and H.A. Enge, Nucl. Instr. and Meth. 49 (1967) 181.

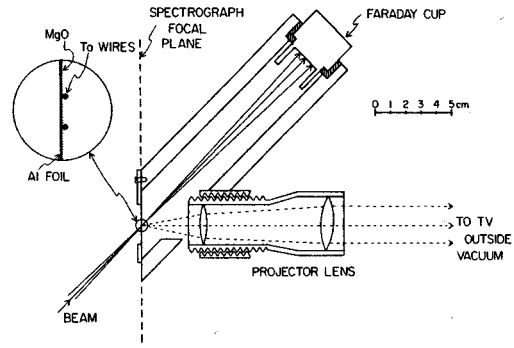

Fig. 1. Viewing apparatus positioned in the spectrograph focal plane. Light from the lens traverses a plastic window before entering the television camera lens. The two vertical wires in the insert, which are 25 μm in diameter and are separated by 2 mm, serve to calibrate the width and relative position of the beam image.

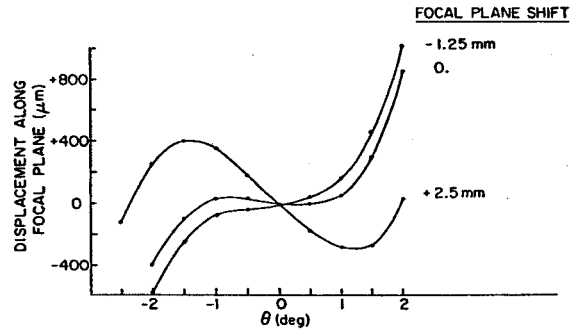

Fig. 2. Image position as a function of spectrograph angle relative to the beam. These data determine the horizontal aberration coefficients y/y'^{2} and y/y'^{3}. Three focal plane positions are shown.

Multiwire Counter Development

R.G. Markham, R.C. Melin, and R.C. Pardo

In the previous annual reports we have discussed the design of a multiwire drift chamber. Its primary characteristics will be the ability to measure angle of incidence and time of arrival as well as to accurately determine the position in the focal plane of the Enge Split-Pole spectrograph.

During the past year the construction and assembly has been completed. Preliminary testing was associated with the high voltage handling characteristics. Some redesign and additions were completed in order to improve the high voltage capabilities. Modifications were guided by using a relaxation code to calculate the electric fields in various geometries. Modifications included adding field shaping planes outside the active area to decrease the fields between the internal components and ground surfaces, adding dielectric material in various locations to prevent surface discharges and shaping the end fields in the counter by the addition of large diameter wires.

In addition, tests were made to determine the best materials to be used as dielectrics. The best materials are those which are most resistant to surface corona discharges. It appears that teflon and G-10 have superior resistance to this type of discharge, with G-10 being chosen as the major construction material due to its better mechanical properties. It also proved necessary to test various epoxies and methods of usage in the fabrication of the detector. Our findings show that a high quality epoxy, mixed to accurate proportions and vacuum pumped to remove a majority of bubbles works very well.

The counter uses pulse transformers as the interconnection between the cathode wires and the preamplifiers. These transformers also terminate the delay line and serve as the means of high voltage isolation. In order to facilitate the high voltage isolation, it was necessary to vacuum impregnate the transformer network in epoxy. The transformers are superior to capacitors in high voltage blocking in that they have negligible stored energy compared to a capacitor to serve the same purpose.

Tests at this time have involved mainly work to allow the detector to be biased to 8KV with a minimum of discharges. Bias tests have proved successful with usable signals being obtained with 35 MeV protons. Preliminary tests of the time resolution look favorable with considerable amounts of time being devoted to the debugging of hardware and also of the software written for the PDP 11/45. Possible modifications include changing the delay line length from 225 nsec total to 450 nsec to make better use of the range of the TDC to improve the coarse position resolution.

A High Resolution, Modular Resistive Wire Counter

L. Robinson

Recent experiments performed in the Enge split-pole Spectrograph, such as the (^{3}He,^{6}He) reaction and heavy ion reactions, have required a position sensitive detector capable of good resolution and also capable of accurate particle identification. A new counter has been built which accomplishes these goals quite well. This counter has a further advantage in being of modular construction; the gas chamber can be opened and closed without the need for changing windows and the scintillator and wire counters are easily replaced or repaired to suit the needs of the user.

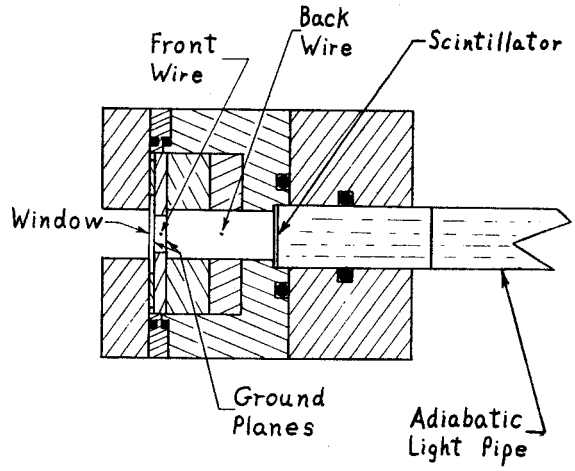

Fig. 1

Fig. 1. A cross-sectional view of the counter. Ground planes are glued to the spacers to permit easy access to the wire supports.

As presently used, the detector consists of:

1) A thin (0.1") wire counter. Since the particles are incident at 45°, ΔE straggling in the gas is the principal limitation of counter resolution. This effect is proportional to $(\frac{t}{Pi})^{\frac{1}{2}}$ where t is counter thickness, P is gas pressure, and i is the ionizing power of the particle, $\frac{dE}{d(\delta x)}$. Therefore a thin counter operating at increased pressure should give improved resolution. The theoretical limit of this counter due to straggling for a 45 MeV ^{6}He particle with 1 atm propane is 0.2 mm. We have actually observed line widths of 0.6 mm, however other effects, such as target thickness, dispersion matching errors, and electronic noise also contributed to the observed width.

2) A thick (0.85") wire counter. ΔE signals from this counter have much better resolution than those from the first counter because of the larger energy loss. This is important for particle identification. The second wire is about 0.5" behind the first, so that a comparison of the two position signals determines the angle at which the particle has traversed the counter. This allows one to eliminate many scattered particles, which go through at the wrong angle and thus give incorrect ΔE signals which contribute to the background. (See Fig. 2).

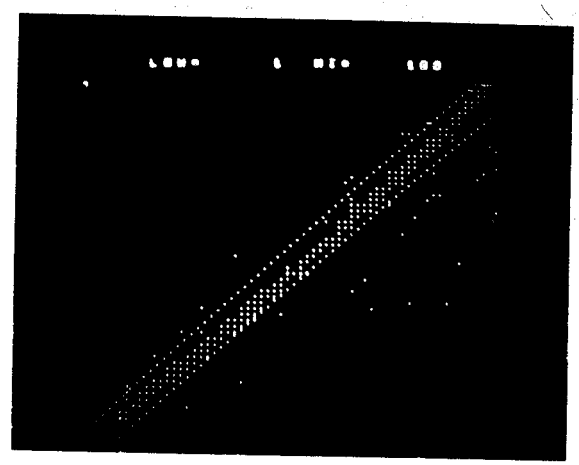

Fig. 2

Fig. 2. A 2-D spectrum obtained with this counter. The x-axis is position on the front counter, the y-axis is position on the back counter. Programmed gates eliminate those counts outside of the two parallel lines.

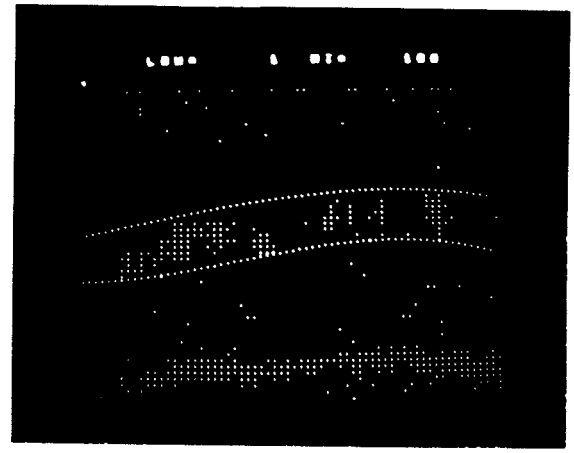

Fig. 3

Fig. 3. The x-axis is position on the front counter, the y-axis is light output. The band is drawn around the ^{6}He particle group. The principal source of background, ^{3}He$^+$, is well separated below the ^{6}He band.

3) A thin (0.039") Pilot-B scintillator. The front surface of the scintillator is coated with approximately 30μg/cm^2 aluminum, which forms a ground plane for the back counter and also reflects light back into the phototube. The

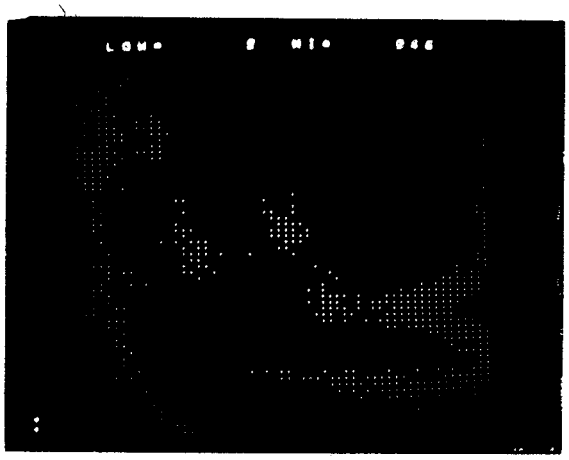

Fig. 4

Fig. 4. A particle spectrum from 75 MeV ^{12}C on ^{58}Ni. The x-axis is E in the back counter, the y-axis is light. Particle groups are identified below.

^{4}He ^{6}Li

^{7}Li ^{9}Be

^{10}Be $^{12}C^{5+}$

scintillator is thick enough to stop particles of interest while background due to gammas and neutrons is low. The scintillator is coupled to the phototube through an adiabatic light pipe. The efficiency of this light pipe is much improved over earlier designs, yielding larger signals and improved light resolution which is crucial to particle identification (Fig. 3, 4).

Sputtering Gun and Other Developments in the Target Laboratory

D. Cole, M. Curtin, J.A. Nolen, Jr., and R.G.H. Robertson

Significant improvements in the target making laboratory made during the last year include construction and operation of a stable and efficient ion sputtering gun, the construction and utilization of two high capacity target storage units featuring dry nitrogen environments, construction of carbon foil production equipment, operational testing of the Cahn microbalance, and production of several targets new to this laboratory.

A simple and economical Ar^+ ion beam sputtering gun developed by Nolen, Curtin, and Dyson[1] was put into operation in 1977. Targets of separated isotopes Pt and Mo as well as natural W, Zn, Ti, and Si were made. While our main goal in sputtering is the production of foils of refractory metals such as W, the sputtering method has proven valuable in the efficient production of targets of high vapor pressure metals such as Cd and Zn. This original sputtering gun was a significant development, but extensive changes were made in 1978, producing a more efficient and more economical gun. The original gun, machined from boron nitride, was replaced by a gun manufactured from a modified ceramic vacuum electrical feedthrough (see figure). The present gun is more

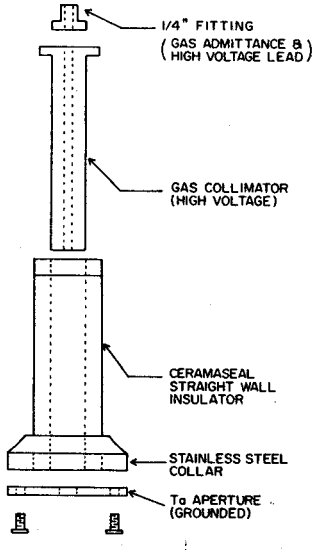

FIG. 1. The components of the present ion beam sputtering gun.

economical, requires less machining time, and is easily removable for quick cleaning. Targets prepared from ^{92}Mo and natural Cd and Zn have also shown this sputtering gun to sputter more efficiently than the original gun, requiring significantly less time to produce like thicknesses. The present sputtering gun is and will remain in general operation for some time, although extensive changes are already being considered.

In the last year, target storage space for both targets classified nonreactive and semi-reactive was exhausted. Also, the roughing pump vacuum semi-reactive target storage proved clumsy and risky with several targets being broken as a result of equipment faults and accidental procedural error. This situation prompted the design and construction of a continuously flowing dry nitrogen target storage unit. The unit features a slightly above atmospheric pressure dry nitrogen environment that has proven safe for most semi-reactive targets and allows little contamination from the room air when opened. Sliding doors are used to minimize air currents when the storage unit is opened. Indicating dessicant lines the unit floor to absorb excess moisture and quickly show up unit malfunction. Each unit has a 250-target capacity. The two units now in use, along with the high vacuum storage unit, brings total target storage capacity to 590 spaces. A third dry nitrogen unit is under construction to allow an additional 250 spaces for future expansion.

Commercial carbon foils of 2-200 $\mu g/cm^2$ have been purchased routinely by this laboratory for several years. Over the last few years the general quality and in particular the uniformity of these foils have become questionable. Recent dissatisfaction with the foils has been responsible for the construction of a carbon arc setup for the manufacture of uniform carbon foils to be used as target backings. The setup designed by L. Robinson uses two high purity carbon rod electrodes and has successfully produced easily floatable and uniform carbon foils of 20-50 $\mu g/cm^2$. The setup, although operational, still requires equipment and procedural development to extend arc life and accurately gauge foil thickness.

Completion of equipment modification and construction has brought the Cahn microbalance to an operational stage. Special evaporator electrodes and masking accessories allow the deposit of target material in a well defined area while shielding the balance from heat and contamination. In initial operational tests gold was evaporated from a tantalum dimple boat and deposited on a substrate suspended from one arm of the microbalance. The evaporation of gold was done in several stages. At each stage the microbalance registered mass increases compatible with deposit appearance. The mass of the gold test deposit was easily measurable to within 20 μg. The stage evaporations and mass measurements were all done over a short time without requiring the system to be let up to air. The ability to measure the target mass and modify it as desired should be of great value in the manufacture of many targets with well defined thicknesses. At this point the microbalance requires mainly procedural development.

Approximately 150 targets were made in our laboratory. While most targets were made using evaporation by resistive heating, an increasing number are being manufactured by electron bombardment or ion sputtering. One technique utilizing both resistive heat evaporation and ion sputtering is now being used to produce Cd and Zn targets. Both metals must be reduced from their oxides for use. Attempts to reduce and evaporate these high vapor pressure metals onto substrates result in deposits on everything but the substrates. Suitable targets can be made by reducing and evaporating the metal from a Ta boat, condensing it onto a water cooled copper block, and finally sputtering the freed deposit onto a substrate. Because the ion beam sputtering system gives much higher deposition velocities than thermal evaporation, the sticking probability is essentially unity even for Zn and Cd.

---

1. J.A. Nolen, Jr., M.S. Curtin, and T.E. Dyson, Nucl. Instr. and Meth. 150 (1978) 581.

Table I. New targets and targets made using new techniques are listed below.

Target Element	Chemical Form of Target	Starting Material	Method of Fabrication	Backing[1]	Thickness ($\mu m/cm^2$)	Amount of Isotope Required for 100 $\frac{\mu g}{cm^2}$	Remarks
Zn	Zn	ZnO	Vacuum Evaporation & ion sputtering	C	≈ 300	< 1.0	Two stage
Cd	Cd	CdO	Vacuum evaporation & ion sputtering	C	≈ 1000	< 1.0	Two stage
C	C	C	Carbon arc setup	S.S.	20-50	--	BaCl floatation
^{170}Er	^{170}Er	Er_2O_3	Electron bomb, Ta crucible with Th powder	S.S.	≈ 9000	0.3	Ta substrate dissolved in HF
^{92}Mo	^{92}Mo	^{92}Mo	Ion sputtering	C	40-150	< 1.0	
Lu	Lu	Lu_2O_3	Vacuum evaporation,[3] Ta point source, with Ta powder	C	100	≈ 15.0	
Pr	Pr	Pr_2O_3	Vacuum evaporation,[3] Ta point source, with Ta powder	C	100	≈ 15.0	
Ba	Ba	$Ba(CO_3)$	Vacuum evaporation,[3] Zr point source,[2] with Zr powder	C	25	≈ 6.0	
U	UF_4	UF_4	Electron bomb.	C	100	≈ 2.0	
Se	Se	Se	Vacuum evaporation Ta, W dimple boat		100	≈ 4.0	Deposit on detector window
NaI	NaI	NaI	Vacuum evaporation, W dimple boat	C	150	≈ 4.0	
^{6}LiF	^{6}LiF	^{6}LiF	Vacuum evaporation, W dimple boat	Formvar	20	≈ 4.0	

1. S.S. refers to self-supporting targets and C usually means 20 $\mu g/cm^2$ carbon plus formvar.
2. Ta and Zr point source means tube with ends smashed and small hole drilled in its side.
3. Simultaneous reduction and evaporation.

Field Calculations for the SIEGFRIED Mass Identification System

M. Distasio, R.B. Firestone, and Wm. C. McHarris

Our investigations into the details of mass spectra obtained with SIEGFRIED, a recoil-mass time of flight system, have revealed some interesting results and potentially useful measurements of decay parameters. Shown in figure 1 is a mass spectrum resulting from 70 MeV ^{3}He on ^{27}Al, the abscissa is recoil energy.

The peaks corresponding to masses 24-27 amu all have very similar shapes, long nearly exponential tails on the high energy side and then a sharp cut off. Comparison of these shapes with theoretical recoil energy distributions, shown in Fig. 2, demonstrates that the experimental shapes are the reverse of the theoretical.

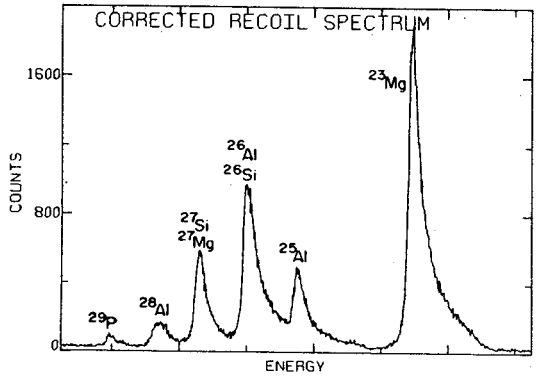

Fig. 1. Recoil Mass Spectrum Obtained with SIEGFRIED.

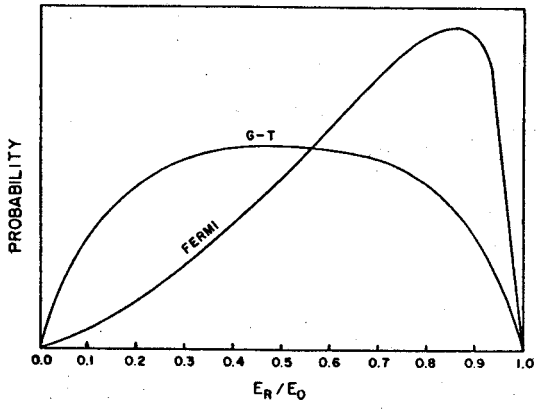

Fig. 2. Theoretical Recoil Energy Distributions

In an attempt to explain the skewed results we are in the process of calculating particle trajectories through the spectrometer, which utilizes purely electrostatic accelerating and focusing elements. In order to obtain a quantitative map of the electric fields in the device, we have used the method of successive overrelaxation to solve Laplace's equation with the appropriate boundary conditions.

In figure 3 equipotentials, calculated for the region where particles are accelerated, are shown. The shaded area is an insulating support; as is apparent from the figure the acceleration is primarily in the Z direction.

Equipotentials corresponding to a prototype of the flight path, are shown in figure 4. Centered along the Z axis is a particle guide wire held at -110 V, that acts to focus the particles to the position of a detector at the right end of the wire. Regions of defocusing and longitudinal accelerations, that tend to broaden the mass peaks, are clearly shown in figure 4.

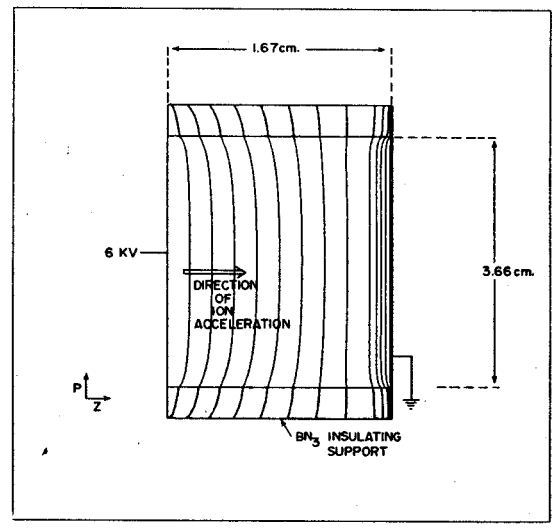

Fig. 3. Calculated Equipotentials for the Acceleration Region.

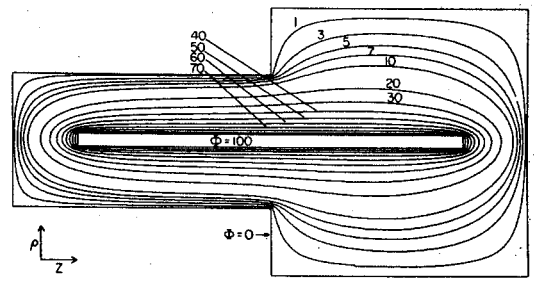

Fig. 4. Equipotentials for a Prototype of the Flight-Path Region.